Intrinsic catalytic properties of histone H3 lysine-9 methyltransferases preserve mono-methylation levels under low *S*-adenosylmethionine

Spencer A. Haws[1,2], Lillian J. Miller[1,2], Diego Rojas La Luz[3], Vyacheslav I. Kuznetsov[1,2], Gheorghe Craciun[2,3], and John M. Denu[1,2]

[1]Wisconsin Institute for Discovery, University of Wisconsin-Madison, Madison, Wisconsin
[2]Department of Biomolecular Chemistry, SMPH, University of Wisconsin-Madison, Madison, Wisconsin
[3]Department of Mathematics, University of Wisconsin-Madison, Madison, Wisconsin

ABSTRACT

Histone methyltransferases (HMTs) rely on *S*-adenosylmethionine (SAM) as a methyl-donor to perform site-specific methylation of histone lysine residues. During SAM depletion, global di- and trimethylation of histone lysines are reduced, whereas monomethylation, particularly at histone H3 lysine-9 (H3K9), is actively maintained. Here, we investigate whether the intrinsic properties of H3K9 HMTs could explain these methylation preferences observed *in vivo*. We employed a systematic steady-state kinetic and substrate binding analysis of four nuclear H3K9 HMTs (i.e., EHMT1, EHMT2, SUV39H1, and SUV39H2) using methylated forms of H3 substrates as a function of varied SAM concentrations. These HMTs displayed highest catalytic efficiency for mono- relative to di- and trimethylation under SAM limiting ($k_{cat}/K_{M,\ SAM}$) conditions. Under saturating conditions of both SAM and H3 substrate, EHMT1, EHMT2, and SUV39H1 also favor monomethylation while SUV39H2 displays a similar k_{cat} with each subsequent methylation. Under varied H3 concentrations, the resulting $k_{cat}/K_{M,\ H3}$ indicate 1-2 orders of magnitude increase for monomethylation compared to trimethylation. Binding studies show all four enzymes exhibit relatively small differences in affinity between H3K9 methylation states, suggesting strong substrate discrimination occurs during catalysis. Using a time-course of cellular SAM depletion and mass spectrometry-based measurements of nuclear H3K9 methylation states, we built a mathematical model to investigate whether the intrinsic catalytic rates could explain the observed nuclear methylation dynamics. Indeed, the model accurately simulates the dynamics of all H3 methylation states previously observed during SAM depletion. Best fits to the model reveal H3K9 methylation is the major draw of cellular SAM and that a small emergency supply is required after >90% SAM depletion. The results of this study suggest that the intrinsic enzymatic activity of H3K9 methyltransferases have evolved to maintain monomethylated pools of H3 when SAM levels are dramatically perturbed.

INTRODUCTION

Histone lysine methylation is an epigenetic post-translational modification (PTM) catalyzed by histone methyltransferases (HMTs) on the ε-amino group of lysine residues. Histone lysine residues can be utilized as platforms for three distinct methylation states (mono-, di-, and trimethylation), that along with the location and amino acid sequence surrounding the lysine residue, confer distinct biological function [1]. For example, H3 Lys-4 monomethylation (H3K4me1) is known to mark active or primed enhancers, while H3 Lys-27 trimethylation (H3K27me3) at gene promoters is associated with transcriptional repression [2–7]. The specific site and degree of histone methylation is largely dependent on the depositing HMT(s) which have specificities in both respects, enabling tight regulation over a cell's histone methylation profile [8].

Although there are essential functional differences that distinguish lysine HMTs from one another, all require *S*-adenosylmethionine (SAM) as the methyl-donor cofactor. SAM is the enzymatic product of a synthetase reaction between the essential amino acid methionine and ATP, which is the only known mechanism supporting intracellular SAM availability in higher eukaryotes [9,10]. This reliance on intracellularly derived SAM to support HMT activity creates an interdependence between metabolism and the epigenome [11,12]. Various studies have highlighted this relationship, illustrating how impaired SAM metabolism negatively impacts histone methylation abundance in both isolated cell and whole organism model systems. Interestingly, all forms of histone methylation are not equally sensitive to decreased SAM availability, with di- and trimethyl PTMs generally possessing greater sensitivity than monomethyl PTMs [13–15]. It is hypothesized the sensitivity or robustness of histone methylation to fluctuations in SAM availability may be explained by the inherent catalytic properties of HMTs [16,17]. Biochemical analyses of HMTs report that an increase in substrate methylation state can lead to a corresponding decrease in enzyme catalytic efficiency [18–24], but it is unclear how alterations in SAM levels affect the relative rates of mono-, di- and tri-methylation. Therefore, a detailed comparative analysis is needed to comprehensively determine how metabolic fluctuations in SAM availability impact HMT catalysis on substrates with different degrees of lysine methylation.

In this study, we compare the inherent catalytic properties of four H3 Lys-9 (H3K9) HMTs by employing detailed biochemical analyses that include steady-state kinetics and quantitative binding assays using histone peptide substrates covering the entire range of H3K9 methylation states (i.e., unmodified through dimethylated). The H3K9 HMTs assessed in this study represent two distinct groups of enzymes: EHMT1/ EHMT2 and SUV39H1/SUV39H2. EHMT1 (also known as GLP, G9a-like protein) and EHMT2 (also known as G9a) are the primary nuclear H3K9 mono-/di-methyltransferases, best known for regulating facultative heterochromatin and subsequent gene repression [25–28]. SUV39H1 and SUV39H2 are reported to catalyze nuclear H3K9 di- and trimethylation, requiring a previously methylated substrate, and regulate constitutive heterochromatin formation and maintenance [29–32]. These functions are critical for the repression of repetitive and retrotransposable elements as well as 3-dimensional chromosome compartmentalization [33]. By assessing the biochemical characteristics of these enzymes in a single study and subsequently incorporating these results into a mathematical model of nuclear H3K9 methylation dynamics, we develop an accurate model that can explain the methylated states under rapid loss of intracellular SAM.

RESULTS

H3K9 monomethylation is the most catalytically efficient methyltransferase reaction under SAM limitation

We previously demonstrated that the levels of monomethylation at H3K9 and H3K27 are held steady during severe intracellular SAM depletion while tri- and di-methylation of most histone lysine sites are dramatically reduced [[13]]. Genetic and pharmacological knockdown of H3K9 mono-methyltransferases EHMT1/ EHMT2 blocked the ability of cells to sustain both global and loci-specific PTM levels that are critical for the preservation of heterochromatin stability during this metabolic stress. However the mechanism(s) by which monomethylation is favored under extremely low SAM levels is unknown. One potential explanation for these results is that low intracellular SAM levels lead to HMT activity that favors mono-methylation over high-order states. To begin uncovering the mechanism(s) supporting active histone monomethylation in the presence of reduced SAM availability, we determined how SAM availability (i.e., concentration dependence) influences each form of histone lysine methylation catalysis (i.e., mono-, di-, and trimethylation). This was accomplished by assessing the steady-state kinetic properties of recombinantly purified H3K9 HMTs that included the *in vivo* H3K9me1/me2 HMTs EHMT1 and EHMT2 as well as the *in vivo* H3K9me2/H3K9me3 HMTs SUV39H1 and SUV39H2.

First, we measure steady-state catalytic rates at varied SAM concentrations and fixed, saturating concentrations of three different H3 peptide substrates covering the entire range of potential substrate methylation states (H3K9un, H3K9me1, and H3K9me2). We fit the resulting data to the Michaelis-Menten equation to obtain steady-state parameters k_{cat}, k_{cat}/K_M and K_M. At saturating SAM conditions, a comparison of the k_{cat} values indicates substrate turnover generally decreases as H3 peptide methylation state increases for EHMT1, EHMT2 and SUV39H1 (Figure 1A, Table 1). The transition from unmodified to monomethylated substrate yields the greatest reduction in EHMT1 and EHMT2 k_{cat} rates (i.e., 12.7 to 2.01 min^{-1} and 7.62 to 2.15 min^{-1}, respectively) while SUV39H1 is most negatively impacted by the transition from mono- to dimethylated substrate (i.e., 0.30 to 0.03 min^{-1}) (Figure 1C-E). Interestingly, SUV39H2 substrate turnover rates are largely unaffected by H3 peptide methylation status, although k_{cat} values for SUV39H2 are consistently below those of EHMT1 and EHMT2 when all enzymes are provided with an unmodified substrate (Figure 1F). Thus, at saturating SAM levels, all four enzymes display maximal turnover for monomethylation of the unmodified peptide.

Although H3K9 monomethylation is the most enzymatically favorable reaction under saturating levels of both SAM and H3 substrates, it is critical to understand the intrinsic methylation rates when SAM is present at very low concentrations such as in cellular conditions of SAM depletion. For this evaluation, we compare $k_{cat}/K_{m,\,SAM}$ values amongst each HMT and substrate methylation state combination (Figure 1B, Table 1). The $k_{cat}/K_{M,\,SAM}$ parameter is the intrinsic catalytic efficiency of the enzyme when SAM levels are limiting. The $k_{cat}/K_{M,\,SAM}$ values reveal the transition from unmodified to monomethylated substrate result in the greatest reduction in catalytic efficiency for EHMT1 (i.e., 1.01 to 0.30 min^{-1} μM^{-1}), EHMT2 (i.e., 0.40 to 0.13 min^{-1} μM^{-1}), and SUV39H2 (i.e., 0.86 to 0.36 min^{-1} μM^{-1}) (Figure 1C-D and 1F). SUV39H1 also displayed this consistent ~3-fold reduction in

catalytic efficiency when transitioning from unmodified to monomethylated substrate (i.e., 0.10 to 0.03 min^{-1} μM^{-1}) (Figure 1E). However, SUV39H1 distinctly displays an additional ~3-fold reduction in catalytic efficiency when transitioning from mono- to dimethylated substrate while all other enzymes display either no change (i.e., EHMT1) or a slight increase (i.e., EHMT2 and SUV39H2).

Together, these data show increased catalytic efficiency for H3K9 mono- relative to di- and trimethylation is a conserved feature of H3K9 HMTs under SAM limiting ($k_{cat}/K_{M,\ SAM}$) conditions. Under SAM saturating conditions (k_{cat}), EHMT1, EHMT2, and SUV39H1 favor monomethylation reactions by 6.4-, 3.5-, and 1.4-fold over dimethylation, and by 19-, 7-, and 14-fold over trimethylation, respectively. In stark contrast, SUV39H2 displays a similar k_{cat} value of ~4 min^{-1} for all three substrates. These data suggest that for all methyltransferases except SUV39H2, there is strong substrate discrimination that occurs after both SAM and histone have bound.

Assessment of H3K9 proteoform availability and the intrinsic catalytic properties of HMTs.

Thus far in the analysis, steady-state kinetic properties suggest H3K9 HMTs intrinsically prefer H3K9 mono- over both di- and trimethylation at both limiting and saturating levels of SAM, reflected in $k_{cat}/K_{M,\ SAM}$ and k_{cat}, respectively. The notable exception is SUV39H2 which displays no difference in turnover (k_{cat}) amongst the possible histone substrates. While these conclusions hold at saturating levels of the various methylated peptides, it is important to consider the levels of distinct H3K9 methyl-proteoforms *in vivo* which fluctuate in response to SAM deprivation. Therefore, it is instructive to determine the intrinsic catalytic efficiency for methylation at non-saturating levels of each substrate, which is reflected in the k_{cat}/K_M value for histone substrates. To obtain a more physiological perspective on the kinetic preferences for histone methylation targets *in vivo*, we calculated the estimated concentrations of various H3K9 methylation states under SAM abundance and depletion conditions using previously quantified relative amounts of K9un, K9me1, K9me2 and K9me3 [13]. Utilizing the LC-MS/MS stoichiometry values previously determined using HCT116 colorectal cancer cells, we first calculated the theoretical concentration of nucleosome incorporated H3 proteins within the nucleus. This was accomplished by dividing the total base pair (bp) length of the diploid *H. sapiens* reference genome hg38.p13 (including an X and Y chromosome) by 166 bp (146 bp bound + 20 bp linker DNA per nucleosome) to estimate the number of nucleosomes present in a single nucleus. Upon converting the total number of nucleosomes to a mass value of total H3 proteins, we used an estimated nuclear volume for HCT116 cells calculated with a previously published diameter to determine the theoretical concentration of H3 proteins within the nucleus. Our theoretical nuclear H3 protein concentration of ~170 μM was comparable to those previously reported from other cell types [34,35]. By applying this theoretical concentration to our published H3K9 proteoform stoichiometry data, we generated H3K9 proteoform specific concentrations under both SAM-replete and -deplete conditions (Table 2). This analysis reveals SAM depletion stimulates low- to mid-micromolar fluctuations in H3K9un (i.e., 19.5 to 39.6 μM) and H3K9me2 (i.e., 63.7 to 26.8 μM) abundance while H3K9me1 concentrations remained relatively constant (i.e., 24.7 to 21.1 μM) (Figure 2A-C).

With good estimates in hand for the full range of H3K9 methyl-proteoform substrates present under extreme SAM fluctuations, we determine the relevant kinetic parameters ($k_{cat}/K_{M,\ PEPTIDE}$ and $K_{M,\ PEPTIDE}$) for the various methylated peptides and assess how these rates are critical for understanding H3K9 HMT activity *in*

vivo. Here, we varied the concentrations of each H3K9 proteoform peptide at a saturating SAM concentration, determined the steady-state rates for all four HMTs, and fit the data to the Michaelis-Menten equation to obtain the relevant parameters (Table 3). The $K_{M,\ H3K9un}$ and $K_{M,\ H3K9me1}$ values for each enzyme are all a minimum of ~5-fold below estimated *in vivo* proteoform concentrations both pre- and post-SAM depletion (Figure 2A-B and Figure 3C-F). The $K_{M,\ H3K9me2}$ values for EHMT2, SUV39H1, and SUV39H2 are all at least ~6-fold below the pre-SAM depletion *in vivo* proteoform concentration estimates but only at or more than ~2.5-fold below our post-SAM depletion estimate (Figure 2C and Figure 3D-F). This suggests histone substrate concentrations of all three methylated species are near saturating even under SAM depleted conditions, and importantly, predicts that *in vivo* rates of methylation are dictated by each enzyme's intrinsic turnover rate, when SAM is saturating. Interestingly, the EHMT1 $K_{M,\ H3K9me2}$ value (i.e., 64.57 μM) is significantly greater than those for the other enzymes (Table 3). This $K_{M,\ H3K9me2}$ value is similar to pre-SAM depletion proteoform levels (i.e., 63.7 μM) while being greater than post-SAM depletion proteoform levels (i.e., 23.77 μM), suggesting EHMT1 is not saturated by this substrate *in vivo* (Table 2). These data suggest that *in vivo,* low SAM conditions further disfavor H3K9 trimethylation by EHMT1.

Analysis of the k_{cat}/K_M values for unmodified, mono- and dimethylated H3K9 substrates reveals a generally larger intrinsic preference for unmodified and monomethylated substrates than observed with k_{cat} values alone among the four enzymes (Table 3). Consistent with the trends in k_{cat} values, EHMT1 is the most selective for lower methylated substrates, while SUV39H2 is the least selective. To investigate if the extent of methylation of the H3K9 ε-amino group weakens interactions with the HMTs, we used fluorescence polarization (FP) assays to generate dissociation constants (K_d) for each possible combination of H3K9 proteoform and HMT. We perform the assays by titrating enzyme concentrations with fixed concentrations of FAM-labeled H3 peptides in the presence of *S*-adenosylhomocysteine (SAH), the metabolic product of SAM-dependent methyltransferase reactions. Interestingly, we find the methylation state-dependent trends in K_d values are distinctly different for EHMT1 and EHMT2 compared to SUV39H1 and SUV39H2 (Table 4). Sequential addition of methyl groups to the H3K9 residue yields a corresponding increase in K_d values for both EHMT1 (i.e., H3K9un = 0.029 μM, H3K9me1 = 0.074 μM, H3K9me2 = 0.124 μM) and EHMT2 (i.e., H3K9un = 0.016 μM, H3K9me1 = 0.026 μM, H3K9me2 = 0.04 μM). However, the relatively small 1.5-2.6 fold-change increase in K_d values following each methyl-group addition are significantly lower in magnitude than the fold-change effects on k_{cat}/K_M with increasing peptide methylation of the starting substrate. Given the caveat that these binding assays reflect peptide binding to a deadend product complex with SAH, these data suggest differences in H3 peptide affinity do not account for the larger catalytic efficiency differences for EHMT1 and EHMT2 as substrate methylation status increases. Instead, these data support catalytic discrimination for lower methylation states that exist during chemical catalysis.

Compared to EHMT1 and EHMT2, SUV39H1 and SUV39H2 display almost no effect on K_d values regardless of H3 methylation status (Table 4). The K_d values for both unmodified and dimethylated peptide substrates are comparable (i.e., SUV39H1: H3K9un = 0.499 μM and H3K9me2 = 0.479 μM, SUV39H2: H3K9un = 1.075 μM and H3K9me2 = 0.929 μM). The K_d values for monomethylated substrates are distinct from unmodified and dimethylated K_d values for both enzymes (i.e., SUV39H1: H3K9me1 = 0.75 μM, SUV39H2:

H3K9me1 = 0.694 μM), although differences were minimal. As was the case with EHMT1 and EHMT2, these minor differences in substrate binding affinity upon methyl-group addition are unlikely to account for the larger changes in k_{cat}/K_M observed with SUV39H1 and SUV39H2. Collectively, these data suggest that EHMT1, EHMT2, and SUV39H1 intrinsically favor monomethylation over tri-methylation, whereas SUV39H2 displays little catalytic discrimination. After accounting for small changes in binding affinity, it is clear that the preferences displayed by these enzymes occur after substrate binding and are consistent with steps involving chemical catalysis. This preference holds at both low and high concentrations of SAM. The results presented in this study demonstrate that all intrinsic kinetic parameters of HMTs favor the monomethylation reaction, and that even with the one exception, monomethylation by SUV39H2 is on par with higher-order methylations.

Mathematical modeling guided by HMT kinetic parameters reproduces nuclear H3K9 methylation dynamics during SAM depletion

Given that the intrinsic catalytic properties of HMTs favored monomethylation *in vitro*, we next asked whether these empirically-derived kinetic parameters might accurately predict our previously reported *in vivo* H3K9 methylation dynamics [13]. To accomplish this, we developed and implemented a mathematical model based on coupled differential equations that describe histone methylation and demethylation when SAM levels drop dramatically.

Our model uses the simplest and most common reaction rate functions, which are given by mass-action kinetics [36], as shown below:

$$\begin{aligned}
\frac{dH_0}{dt} &= -k_{01}H_0S + k_{10}H_1 \\
\frac{dH_1}{dt} &= -k_{12}H_1S + k_{01}H_0S - k_{10}H_1 + k_{21}H_2 \\
\frac{dH_2}{dt} &= -k_{23}H_2S + k_{12}H_1S - k_{21}H_2 + k_{32}H_3 \\
\frac{dH_3}{dt} &= k_{23}H_2S - k_{32}H_3 \\
\frac{dS}{dt} &= -k_{01}H_0S - k_{12}H_1S - k_{23}H_2S
\end{aligned}$$

Here the variables H_0, H_1, H_2, H_3 represent the different levels of histone methylation (none, single-, double- and triple-methylation, respectively), and the variable S represents the concentration of SAM. The differential equations take into account the fact that each methylation reaction depends on [SAM] and that one molecule of SAM is consumed at each methylation step. The model parameters are the rate constants for SAM-dependent methylation, and rate constants for demethylation. We impose the restriction that the relative ratios of SAM-dependent methylation parameters $k_{01} : k_{12} : k_{23}$ are in the proportions 3:1:1, which is based on experimentally

measured values of $V/K_{M,\ SAM}$ for EHMT1 and represents a conservative ratio of methylation efficiencies. An additional parameter (not shown in the equations above) allows us to analyze the possibility that the cell responds to the metabolic stress caused by low SAM levels by tapping into a small alternative "emergency supply" of SAM, likely through a methionine salvage pathway. We implement this external source as an inflow that has a small but constant rate. We implement this mathematical model in MATLAB, and use the MATLAB solver *ode45* to calculate numerical solutions. We use these solutions as input into MATLAB's *lsqnonlin* function, together with actual LC-MS/MS measurements (in μM) of H3K9un, H3K9me1, H3K9me2 and H3K9me3 as well as estimated LC-MS levels of SAM in HCT116 human cell line after methionine depletion. Lastly, we use the outputs of the nonlinear least squares optimization algorithm to estimate the values of the parameters in the system, and we use these estimated values to plot the best fit simulation results.

A comparison between actual experimental measurements and numerical simulation results for H3K9un, H3K9me1, H3K9me2, H3K9me3, and SAM shows the model can fit the experimentally measured histone methylation levels and SAM levels over the full 24 hours, if we assume the possibility of an small external "emergency supply" of SAM, as described above (Figure 4A). If performing experimental measurements at smaller time intervals over only the first 90 minutes, we see that the general trends of the simulation results continue to follow the experimental results (Figure 4B). Importantly, removing the "emergency supply" of SAM has a significant negative impact on the overall fit of our model over the entire time course (Figure 4C), highlighting the importance of this accompanying mechanism in regulating nuclear H3K9 methylation under severe SAM limitation.

DISCUSSION

Here, the biochemical properties of two functionally distinct pairs of H3K9 HMTs were assessed using *in vitro* steady-state kinetics and quantitative substrate binding assays. We found that greater HMT catalytic efficiency for mono-methylation relative to di- and tri-methylation reactions dictates H3K9 methylation when SAM is limited. In addition, k_{cat} and k_{cat}/K_M values for peptide generally favor mono-methylation of H3. These analyses reveal a fundamental property of H3K9 HMTs and suggest an evolutionary pressure to ensure mono-methylation of H3. To demonstrate the physiological implications of these *in vitro* analyses, we utilized mathematical modeling of nuclear H3K9 proteoform dynamics guided by the kinetic parameters generated here to reproduce our previous *in vivo* observations. Together, these data reveal the intrinsic catalytic properties of H3K9 histone methyltransferases are largely sufficient to explain changes in nuclear H3K9 methylation profiles under severe SAM depletion. Also, the rapid drop in SAM levels (via methionine depletion) are likely the direct consequence of H3K9 HMT activity, and the ability to maintain mono-methylation at longer periods of methionine restriction likely results from a small salvaged source of SAM.

In agreement with our enzymatic comparisons, a structural study of the mutated SET domain lysine methyltransferase SET7/9 Y305F also suggests H3K9 di-methylation is less catalytically efficient than mono-methylation [23]. SET7/9 is considered a representative model for studying SET domain catalysis while the Y305F construct mimics the presence of a critical active site phenylalanine residue in the nuclear HMTs studied here

[22,37,38]. Specifically, Rizzo et al., 2010 determined an active site water molecule positions the unmodified lysine substrate ε-amino group for nucleophilic attack of the SAM sulfur atom [23]. The water molecule positions the lysine ε-amino group by facilitating a network of four hydrogen bonds between active site residues and the peptide substrate. However, the active site water molecule is lost when SET7/9 Y305F is provided with a monomethyl lysine due to steric limitations. Loss of the active site water molecule frees a solvent pocket for the monomethyl lysine to reside in, ultimately positioning the ε-amino group for nucleophilic attack of the SAM molecule. This loss of water molecule-substrate coordination for monomethyl lysine residues is the proposed mechanism driving significant decreases in catalytic efficiency for SET7/9 mutant Y305F for K189me1 on substrate TAF10 compared to unmodified K189 substrate [23].

In the current study, we focused on the potential differences between two classes of nuclear HMTs, investigating the catalytic mechanisms of the major *in vivo* contributors to H3K9 mono- and di-methylation (i.e., EHMT1/EHMT2) and di- and tri-methylation (i.e., SUV39H1/SUV39H2). Other HMTs not characterized here have also been shown to perform H3K9 mono-methylation *in vivo,* such as SETDB1 in addition to the proposed cytoplasmic HMTs PRDM3 and PRDM16 [32,39]. The SET domain of SETDB1 contains all highly conserved residues present in the enzymes assayed in this study, suggesting similar trends in efficient catalysis of H3K9 mono-methylation. In contrast, PRDM3 and PRDM16 lack the final tyrosine residue of the consensus ELxF/YDY SET domain sequence which has both structural and catalytic importance in canonical SET domain-containing HMTs [19,40–42]. Therefore, PRDM3 and PRDM16 require a dedicated study to better understand how their catalytic activity may contribute to meaningful levels of H3K9me1 *in vivo*.

While the current study employed synthetic H3 peptides to carry out a rigorous analysis of the steady state kinetics and equilibrium binding experiments, it is important to point out the strengths and potential limitations of such studies. One might argue that our studies are limited in physiological relevance because we did not use nucleosomal substrates in our *in vitro* analysis. While this is certainly a fair concern, there are a number of reasons the use of peptides in this study was a tremendous advantage over the use of mononucleosomes. Peptides allowed us to perform detailed saturation kinetics with 4 different methylated forms of H3 and with extremely high accuracy and precision. This would have been nearly impossible with nucleosomes. Also, the fact that discrimination of the various methylated forms of H3 occurred during catalysis and not within the Michaelis complex strongly suggests that the H3 tail and the accompanying K9 methylation are the key features of catalysis. Moreover, the validation (via a mathematical model) that the kinetic parameters determined in this study were able to reproduce *in vivo* observations, provide strong additional evidence that the described *in vitro* behavior of HMTs recapitulates nucleosome methylation under severe SAM limitation. Nevertheless, it is important to note that interactions with a nucleosomal substrate may result in conformational changes to an HMT which could impact its catalytic properties. Sanchez et al., 2021 reported that an EHMT1/EHMT2 heterodimer possesses an unmodified peptide substrate k_{cat} ~800-fold greater than the k_{obs} for unmodified nucleosomal substrates [21]. Importantly, the EHMT1/EHMT2 heterodimer was shown to possess similar binding affinities for both unmodified peptide (K_d = 7.35 μM) and nucleosomal (K_d = 6.50 μM) substrates, consistent with our observation that HMT turnover of differentially methylated substrates is driven by inherent catalytic properties toward the histone tail and not through binding preferences [21].

REFERENCES

1. Millán-Zambrano, G., Burton, A., Bannister, A. J. & Schneider, R. Histone post-translational modifications — cause and consequence of genome function. *Nat Rev Genet* **23**, 563–580 (2022).
2. Heintzman, N. D. *et al.* Histone modifications at human enhancers reflect global cell-type-specific gene expression. *Nature* **459**, 108–112 (2009).
3. Heintzman, N. D. *et al.* Distinct and predictive chromatin signatures of transcriptional promoters and enhancers in the human genome. *Nat Genet* **39**, 311–318 (2007).
4. Rada-Iglesias, A. *et al.* A unique chromatin signature uncovers early developmental enhancers in humans. *Nature* **470**, 279–283 (2011).
5. Local, A. *et al.* Identification of H3K4me1-associated proteins at mammalian enhancers. *Nature Genetics* **50**, 73–82 (2018).
6. Barski, A. *et al.* High-resolution profiling of histone methylations in the human genome. *Cell* **129**, 823–837 (2007).
7. Margueron, R. & Reinberg, D. The Polycomb complex PRC2 and its mark in life. *Nature* **469**, 343–349 (2011).
8. Hyun, K., Jeon, J., Park, K. & Kim, J. Writing, erasing and reading histone lysine methylations. *Exp Mol Med* **49**, e324–e324 (2017).
9. Sun, Y. & Locasale, J. W. Rethinking the bioavailability and cellular transport properties of S-adenosylmethionine. *Cell Stress* **6**, 1–5 (2021).
10. Ducker, G. S. & Rabinowitz, J. D. One-Carbon Metabolism in Health and Disease. *Cell Metabolism* **25**, 27–42 (2017).
11. Boon, R., Silveira, G. G. & Mostoslavsky, R. Nuclear metabolism and the regulation of the epigenome. *Nature Metabolism* **2**, 1190–1203 (2020).
12. Haws, S. A., Leech, C. M. & Denu, J. M. Metabolism and the Epigenome: A Dynamic Relationship. *Trends Biochem Sci* **45**, 731–747 (2020).
13. Haws, S. A. *et al.* Methyl-Metabolite Depletion Elicits Adaptive Responses to Support Heterochromatin

Stability and Epigenetic Persistence. *Mol Cell* **78**, 210-223.e8 (2020).

14. Kera, Y. *et al.* Methionine Adenosyltransferase II-dependent Histone H3K9 Methylation at the COX-2 Gene Locus. *J. Biol. Chem.* **288**, 13592–13601 (2013).

15. Tang, X. *et al.* Comprehensive Profiling of Amino Acid Response Uncovers Unique Methionine-Deprived Response Dependent on Intact Creatine Biosynthesis. *PLOS Genetics* **11**, e1005158 (2015).

16. Dai, Z., Ramesh, V. & Locasale, J. W. The evolving metabolic landscape of chromatin biology and epigenetics. *Nature Reviews Genetics* **21**, 737–753 (2020).

17. Mentch, S. J. & Locasale, J. W. One-carbon metabolism and epigenetics: understanding the specificity. *Annals of the New York Academy of Sciences* **1363**, 91–98 (2016).

18. Chin, H. G., Patnaik, D., Estève, P.-O., Jacobsen, S. E. & Pradhan, S. Catalytic Properties and Kinetic Mechanism of Human Recombinant Lys-9 Histone H3 Methyltransferase SUV39H1: Participation of the Chromodomain in Enzymatic Catalysis. *Biochemistry* **45**, 3272–3284 (2006).

19. Wu, H. *et al.* Structural Biology of Human H3K9 Methyltransferases. *PLOS ONE* **5**, e8570 (2010).

20. Allali-Hassani, A. *et al.* Fluorescence-Based Methods for Screening Writers and Readers of Histone Methyl Marks: *Journal of Biomolecular Screening* (2011) doi:10.1177/1087057111422256.

21. Sanchez, N. A., Kallweit, L. M., Trnka, M. J., Clemmer, C. L. & Al-Sady, B. Heterodimerization of H3K9 histone methyltransferases G9a and GLP activates methyl reading and writing capabilities. *Journal of Biological Chemistry* **297**, (2021).

22. Couture, J.-F., Dirk, L. M. A., Brunzelle, J. S., Houtz, R. L. & Trievel, R. C. Structural origins for the product specificity of SET domain protein methyltransferases. *PNAS* **105**, 20659–20664 (2008).

23. Rizzo, P. A. D. *et al.* SET7/9 Catalytic Mutants Reveal the Role of Active Site Water Molecules in Lysine Multiple Methylation *. *Journal of Biological Chemistry* **285**, 31849–31858 (2010).

24. Schuhmacher, M. K., Kudithipudi, S., Kusevic, D., Weirich, S. & Jeltsch, A. Activity and specificity of the human SUV39H2 protein lysine methyltransferase. *Biochim Biophys Acta* **1849**, 55–63 (2015).

25. Tachibana, M. *et al.* G9a histone methyltransferase plays a dominant role in euchromatic histone H3 lysine 9 methylation and is essential for early embryogenesis. *Genes Dev* **16**, 1779–1791 (2002).

26. Ueda, J., Tachibana, M., Ikura, T. & Shinkai, Y. Zinc finger protein Wiz links G9a/GLP histone methyltransferases to the co-repressor molecule CtBP. *J Biol Chem* **281**, 20120–20128 (2006).

27. Zylicz, J. J. *et al.* Chromatin dynamics and the role of G9a in gene regulation and enhancer silencing during early mouse development. *eLife* **4**,.

28. Jiang, Q. *et al.* G9a Plays Distinct Roles in Maintaining DNA Methylation, Retrotransposon Silencing, and Chromatin Looping. *Cell Rep* **33**, 108315 (2020).

29. Lachner, M., O'Carroll, D., Rea, S., Mechtler, K. & Jenuwein, T. Methylation of histone H3 lysine 9 creates a binding site for HP1 proteins. *Nature* **410**, 116–120 (2001).

30. Peters, A. H. *et al.* Loss of the Suv39h histone methyltransferases impairs mammalian heterochromatin and genome stability. *Cell* **107**, 323–337 (2001).

31. Rice, J. C. *et al.* Histone Methyltransferases Direct Different Degrees of Methylation to Define Distinct Chromatin Domains. *Molecular Cell* **12**, 1591–1598 (2003).

32. Loyola, A. *et al.* The HP1alpha-CAF1-SetDB1-containing complex provides H3K9me1 for Suv39-mediated K9me3 in pericentric heterochromatin. *EMBO Rep.* **10**, 769–775 (2009).

33. Haws, S. A., Simandi, Z., Barnett, R. J. & Phillips-Cremins, J. E. 3D genome, on repeat: Higher-order folding principles of the heterochromatinized repetitive genome. *Cell* **185**, 2690–2707 (2022).

34. Weidemann, T. *et al.* Counting nucleosomes in living cells with a combination of fluorescence correlation spectroscopy and confocal imaging. *J Mol Biol* **334**, 229–240 (2003).

35. Hihara, S. *et al.* Local nucleosome dynamics facilitate chromatin accessibility in living mammalian cells. *Cell Rep* **2**, 1645–1656 (2012).

36. Yu, P. Y. & Craciun, G. Mathematical Analysis of Chemical Reaction Systems. *Israel Journal of Chemistry* **58**, 733–741 (2018).

37. Dillon, S. C., Zhang, X., Trievel, R. C. & Cheng, X. The SET-domain protein superfamily: protein lysine methyltransferases. *Genome Biol* **6**, 227 (2005).

38. Collins, R. E. *et al.* In Vitro and in Vivo Analyses of a Phe/Tyr Switch Controlling Product Specificity of Histone Lysine Methyltransferases *. *Journal of Biological Chemistry* **280**, 5563–5570 (2005).

39. Pinheiro, I. *et al.* Prdm3 and Prdm16 are H3K9me1 Methyltransferases Required for Mammalian Heterochromatin Integrity. *Cell* **150**, 948–960 (2012).

40. Wu, H. *et al.* Molecular Basis for the Regulation of the H3K4 Methyltransferase Activity of PRDM9. *Cell Reports* **5**, 13–20 (2013).

41. Qian, C. & Zhou, M.-M. SET domain protein lysine methyltransferases: Structure, specificity and catalysis. *Cell. Mol. Life Sci.* **63**, 2755–2763 (2006).

42. Smith, B. C. & Denu, J. M. Chemical mechanisms of histone lysine and arginine modifications. *Biochim. Biophys. Acta* **1789**, 45–57 (2009).

TABLE/FIGURE LEGENDS

Table 1: HMT $H3_{(1-17)}$ K9 proteoform Michaelis-Menten constants with titrated SAM availability.

Table 2: Empirically estimated nuclear H3K9 proteoform concentrations.

Table 3: HMT $H3_{(1-17)}$ K9 proteoform Michaelis-Menten constants with titrated peptide availability.

Table 4: HMT $H3_{(1-17)}$ K9 proteoform dissociation constants.

Figure 1: Kinetic analysis of H3K9 HMTs under SAM limiting conditions. Summary plots depicting (*A*) k_{cat} and (*B*) k_{cat}/K_M values derived from steady-state kinetic analysis of EHMT1, EHMT2, SUV39H1, and SUV39H2 when provided with fixed $H3_{(1-17)}$ K9 unmodified (H3K9un), monomethylated (H3K9me1), or dimethylated (H3K9me2) peptide substrate concentrations and varied SAM concentrations. (*C-F*) Individual steady-state kinetic analyses of EHMT1 (25 nM), EHMT2 (25 nM), SUV39H1 (100 nM), and SUV39H2 (25 nM) under fixed $H3_{(1-17)}$K9 concentrations (50 μM) and varied SAM concentrations (0.1 - 100 μM) which provided the summary values presented in panels (*A*) and (*B*).

Figure 2: Comparison of *in vitro* HMT kinetic parameters with nuclear H3K9 proteoform availability. Nuclear (*A)* H3K9 unmodified (H3K9un), (*B)* monomethylated (H3K9me1), and (*C*) dimethylated (H3K9me2) residue concentrations under SAM-replete and -deplete conditions in HCT116 colorectal cancer cells. H3K9 peptide substrate K_M values generated from the kinetic analysis of EHMT1, EHMT2, SUV39H1, and SUV39H2 presented in Figure 3 are superimposed onto each graph to facilitate direct comparison of *in vivo* H3K9 proteoform availability with empirically determined *in vitro* H3K9 peptide proteoform K_M values.

Figure 3: Kinetic analysis of H3K9 HMTs under H3 substrate limiting conditions. Summary plots depicting (*A*) k_{cat} and (*B*) k_{cat}/K_M values derived from steady-state kinetic analysis of EHMT1, EHMT2, SUV39H1, and SUV39H2 when provided with fixed SAM concentrations and varied $H3_{(1-17)}$ K9 unmodified (H3K9un), monomethylated (H3K9me1), or dimethylated (H3K9me2) peptide substrate concentrations. (*C-F*) Individual steady-state kinetic analyses of EHMT1 (25 nM), EHMT2 (25 nM), SUV39H1 (100 nM), and SUV39H2 (25 nM) under fixed SAM

concentrations (50 μM) and varied $H3_{(1-17)}$ K9 peptide concentrations (0.05 - 50 μM) which provided the summary values presented in panels (*A*) and (*B*).

Figure 4: Mathematical modeling of nuclear H3K9 methylation dynamics. (*A*-*C*) Plots depicting changes in H3K9 proteoform and SAM concentrations as measured both empirically via LC-MS-based analyses and by mathematical modeling using the HMT kinetics data generated in this study. A starting SAM concentration of 20 μM was chosen as a representative intracellular value from which relative LC-MS SAM abundance data was converted to μM values. Panels (*A*) and (*B*) display modeled H3K9 proteoform and SAM concentrations under the assumption of an existent emergency SAM supply while the modeled data in panel (*C*) does not include this assumption.

EXPERIMENTAL PROCEDURES

Recombinant Protein Purification

The *H. sapiens* EHMT1 catalytic subunit (Addgene plasmid #51314) and *H. sapiens* SUV39H2 catalytic subunit (Addgene plasmid #25115) *E. coli* expression plasmids used in this study were acquired from Addgene, made possible through a gift by Cheryl Arrowsmith. The *H. sapiens* EHMT2 catalytic subunit *E. coli* expression plasmid used in this study was provided by the laboratory of Peter W. Lewis at the University of Wisconsin-Madison. All remaining histone methyltransferase expression plasmids were generated for this study and will be made freely available from Addgene. HMT amino acids included in expression plasmids are as follows: EHMT1 = 982-1266; EHMT2 = 913-1193; SUV39H1 = full length with N-terminal maltose binding protein; SUV39H2 = 162-410.

Transformed Rosetta™ *E. coli* competent cells were cultured in 1 L of 2XYT media at 37°C to an O.D. 600 of 0.8. IPTG was then added to each culture at a final concentration of 1 mM. Cultures were allowed to grow for 16 hours at 18°C before being harvested and stored at -80°C. Pellets were resuspended in 30 mL Buffer A (50 mM NaPi, 250 mM NaCl, 10 mM imidazole, pH 7.8) and sonicated on ice with 1 mg/mL lysozyme. Lysate was centrifuged at 45,000xg for 45 min and the supernatant was collected. The supernatant was then loaded onto a HisTrap FF nickel column in line with a GE ÄKTA FPLC. After washing the column with 25% Buffer B (50 mM NaPi, 250 mM NaCl, 250 mM imidazole, pH 7.8), protein was eluted using a linear gradient ending in 100% Buffer B and collected. Fractions were analyzed by Coomassie staining of SDS-PAGE gels to assess purity.

Fractions determined to contain the protein of interest were pooled and dialyzed overnight at 4°C in 4 L of HMT dialysis buffer (20 mM HEPES pH 7.5, 300 mM NaCl, 1 mM TCEP, 10% glycerol). Following dialysis, precipitated protein was pelleted by centrifugation at 4°C for 10 min at 18,000xg and the supernatant was collected. Protein concentrations were determined via absorbance values at 280 nm with extinction coefficient corrections. Final protein samples were aliquoted into single-use 0.2 mL PCR tubes and flash frozen in liquid nitrogen prior to long-term storage at -80°C.

Radiometric EZ-Tip Methyltransferase Assay

Michaelis-Menten saturation curves were generated under steady-state conditions with the non-titrated component concentration being present at ≥ 5x K_M specific to each enzyme. $1x10^5$ CPM values were provided by [methyl-^{3}H] SAM in each reaction. Reaction times and enzyme concentrations were optimized for each HMT to ensure substrate turnover remained below 20%. 50 μM H3 peptide was combined with varying SAM concentrations and either EHMT1 (25 nM), EHMT2 (25 nM), SUV39H1 (100 nM), or SUV39H2 (25 nM) in histone methyltransferase (HMT) activity buffer (50 mM HEPES pH 7.9, 0.5 mM DTT, 0.1 mM AEBSF, 2 mM $MgCl_2$, 0.01 % Triton X-100) with a final volume of 20 μL. Reactions were incubated at 30˚C for 20 minutes before quenching with TFA for a final concentration of 2%. Then, the reactions were cleaned using StageTips (i.e. two Attract SPE disks (Affinisep) in a pipette tip) with 200 μL acidified water (0.5% formic acid) and eluted with 100 μL elution buffer (80% acetonitrile, 0.5% formic acid). The eluates were added to 2 mL of Ultima Gold™ LSC Cocktail (Sigma-Aldrich) and counted on a scintillation counter (PerkinElmer). All CPM values were corrected for decreased StageTip capacity when peptide concentrations exceeded 10 μM. (ADD MORE DETAIL)

Michaelis-Menten Constant Calculations

CPM values were converted to rates of product formation (μM/min) and used to generate Michaelis-Menten kinetic constants via GraphPad Prism v9.1.0 via the following equation: Y = Et*kcat*X/(Km + X). Variable definitions are as follows: Y = rate of product formation/enzyme velocity; X = substrate concentration; Et = concentration of enzyme in reaction.

Fluorescence Polarization Peptide Binding Assay

All assay components (i.e., HMT, N-terminus 5-Carboxyfluorescein (5-FAM) labeled peptide, and SAH) were diluted in fluorescence polarization binding buffer (50 mM HEPES pH 7.9, 2 mM $MgCl_2$, 0.5 mM DTT, 0.1 mM AEBSF, 0.01% Triton X-100, 10% glycerol). SAH was present at a final concentration of 100 μM while 5-FAM labeled peptides were present at a constant final concentration in the range of 20-100 nM. Protein concentrations ranged from low-micromolar to nanomolar concentrations. Reactions were assembled in a black low-flange 384-well plate with a 20 μl final volume. Upon addition of diluted enzyme as final reaction component, 384-well plates were sealed and centrifuged at 1,000xg for 30 sec at room temperature. Prepared 384-well plates were loaded into the BioTek Synergy H4 plate reader after which plates were shaken for 10 sec followed by a 10 min incubation at 25°C. Once the incubation was complete, polarization values were calculated using the BioTek Instruments Gen5 v1.11.5 software package.

Peptide Dissociation Constant (K_d) Calculations

Polarization values were exported from BioTek Instruments Gen5 v1.11.5 software and imported into GraphPad Prism v9.1.0 to calculate dissociation constants using the following “One site -- Specific binding” equation: Y = Bmax*X/(Kd + X). Variable definitions are as follows: Y = fluorescence polarization; X = enzyme concentration; Bmax = maximum specific binding; Kd = equilibrium dissociation constant.

Key Resources

REAGENT or RESOURCE	SOURCE	IDENTIFIER
Chemicals, Peptides, and Recombinant Proteins		
HEPES	Gold Biotechnology	Cat# H-400-100
Magnesium Chloride Hexahydrate	Millipore Sigma	Cat# M9272-100G
Sodium Chloride	Millipore Sigma	Cat# S9888-1KG
Glycerol	Thermo Fisher	Cat# G33-4
Acetonitrile	Thermo Fisher	Cat# A996-4
Formic Acid	Millipore Sigma	Cat# F0507-100ML
Trifluoroacetic Acid	Millipore Sigma	Cat# 302031-100ML
Aprotinin	Gold Biotechnology	Cat# A-655-100

Leupeptin Hemisulfate	Gold Biotechnology	Cat# L-010-25
4-(2-Aminoethyl)-benzenesulfonyl-fluoride (AEBSF)	Gold Biotechnology	Cat# A-540-500
Dithiothreitol (DTT)	Gold Biotechnology	Cat# DTT100
Attract SPE Disks C18 47mm	Affinisep	Cat# SPE-Disks-C18-47.T1.20
H3K9 unmodified peptide (5'-ARTKQTARK$_{un}$STGGKAPRW-3')	This paper	N/A
H3K9 mono-methylated peptide (5'-ARTKQTARK$_{me1}$STGGKAPRW-3')	This paper	N/A
H3K9 di-methylated peptide (5'-ARTKQTARK$_{me2}$STGGKAPRW-3')	This paper	N/A
FAM-H3K9 unmodified peptide (5'-FAM-ARTKQTARK$_{un}$STGGKAPRW-3')	This paper	N/A

FAM-H3K9 mono-methylated peptide (5'-FAM-ARTKQTARK$_{me1}$STGGKAPRW-FAM-3')	This paper	N/A
FAM-H3K9 di-methylated peptide (5'-FAM-ARTKQTARK$_{me2}$STGGKAPRW-3')	This paper	N/A
pET28a-LIC-h EHMT1_982-1266	Addgene	N/A
pET28a-LIC-h EHMT2_913-1193	Peter W. Lewis Laboratory	N/A
pET45b-MBP-TEV-hSUV39H1_FL	This paper	N/A
pET28a-LIC-hSUV39H2_162-410	Addgene	Cat# 25115
pET45b-hPRDM3_2-221	This paper	N/A
pET45b-hPRDM16_2-226	This paper	N/A
Ultima Gold™ LSC Cocktail	Sigma-Aldrich	Cat# L8286
Software and Algorithms		
GraphPad Prism v9.1.0	N/A	https://www.graphpad.com/scientific-software/prism/

MATLAB. 9.7.0.1190202 (R2019b)	N/A	https://www.mathworks.com/products/matlab.html

Kinetic/Binding Constant Summary Tables

Table 1. HMT $H3_{(1-17)}$ K9 proteoform Michaelis-Menten constants with titrated SAM availability.

	K_M μM)			k_{cat} (min^{-1})			k_{cat}/K_M (min^{-1} μM^{-1})		
Protein	H3K9un	H3K9me1	H3K9me2	H3K9un	H3K9me1	H3K9me2	H3K9un	H3K9me1	H3K9me2
EHMT1	13.51 ± 4.95	6.84 ± 1.81	2.21 ± 0.65	12.69 ± 0.65	2.01 ± 0.15	0.67 ± 0.02	1.01 ± 0.27	0.30 ± 0.05	0.32 ± 0.08
EHMT2	19.21 ± 2.00	16.80 ± 2.69	6.1 ± 1.03	7.62 ± 0.11	2.15 ± 0.23	1.05 ± 0.07	0.40 ± 0.04	0.13 ± 0.01	0.17 ± 0.03
SUV39H1	4.52 ± 0.49	11.78 ± 3.85	3.60 ± 1.72	0.43 ± 0.04	0.30 ± 0.05	0.03 ± 0.01	0.10 ± 0.02	0.03 ± 0.01	0.01 ± 0.003
SUV39H2	4.70 ± 0.69	9.85 ± 1.21	8.18 ± 3.14	4.01 ± 0.34	3.54 ± 0.23	4.22 ± 0.35	0.86 ± 0.08	0.36 ± 0.03	0.55 ± 0.15

Table 2. Empirically estimated nuclear H3K9 proteoform concentrations.

	Nuclear Concentration (μM)		
	H3K9un	H3K9me1	H3K9me2
+ SAM	19.5 ± 3.39	24.7 ± 4.86	63.7 ± 8.02
- SAM	39.6 ± 1.36	21.1 ± 1.53	26.8 ± 4.96

Table 3. HMT $H3_{(1-17)}$ K9 proteoform Michaelis-Menten constants with titrated peptide availability.

	K_M (μM)			k_{cat} (min^{-1})			k_{cat}/K_M (min^{-1} μM^{-1})		
Protein	H3K9un	H3K9me1	H3K9me2	H3K9un	H3K9me1	H3K9me2	H3K9un	H3K9me1	H3K9me2
EHMT1	1.68 ± 0.13	3.40 ± 0.72	64.57 ± 23.77	11.11 ± 0.32	2.16 ± 0.16	1.26 ± 0.28	6.65 ± 0.72	0.65 ± 0.13	0.02 ± 0.004
EHMT2	3.62 ± 0.87	1.68 ± 0.17	6.51 ± 1.60	9.36 ± 0.59	3.40 ± 0.04	0.48 ± 0.07	2.66 ± 0.46	2.04 ± 0.18	0.08 ± 0.01
SUV39H1	0.60 ± 0.08	1.03 ± 0.14	10.37 ± 2.78	0.61 ± 0.05	0.45 ± 0.06	0.09 ± 0.01	1.03 ± 0.18	0.45 ± 0.02	0.01 ± 0.003
SUV39H2	1.62 ± 0.09	4.26 ± 0.23	8.01 ± 2.95	5.26 ± 0.15	6.52 ± 0.08	3.38 ± 1.12	3.26 ± 0.22	1.53 ± 0.09	0.43 ± 0.11

Table 4. HMT $H3_{(1-17)}$ K9 proteoform dissociation constants.

	K_d (μM)		
Protein	H3K9un	H3K9me1	H3K9me2
EHMT1	0.029 ± 0.001	0.074 ± 0.010	0.124 ± 0.024
EHMT2	0.016 ± 0.0004	0.026 ± 0.001	0.04 ± 0.003
SUV39H1	0.499 ± 0.045	0.750 ± 0.047	0.479 ± 0.123
SUV39H2	1.075 ± 0.226	0.694 ± 0.098	0.929 ± 0.573

Figure 1: Kinetic analysis of H3K9 HMTs under SAM limiting conditions.

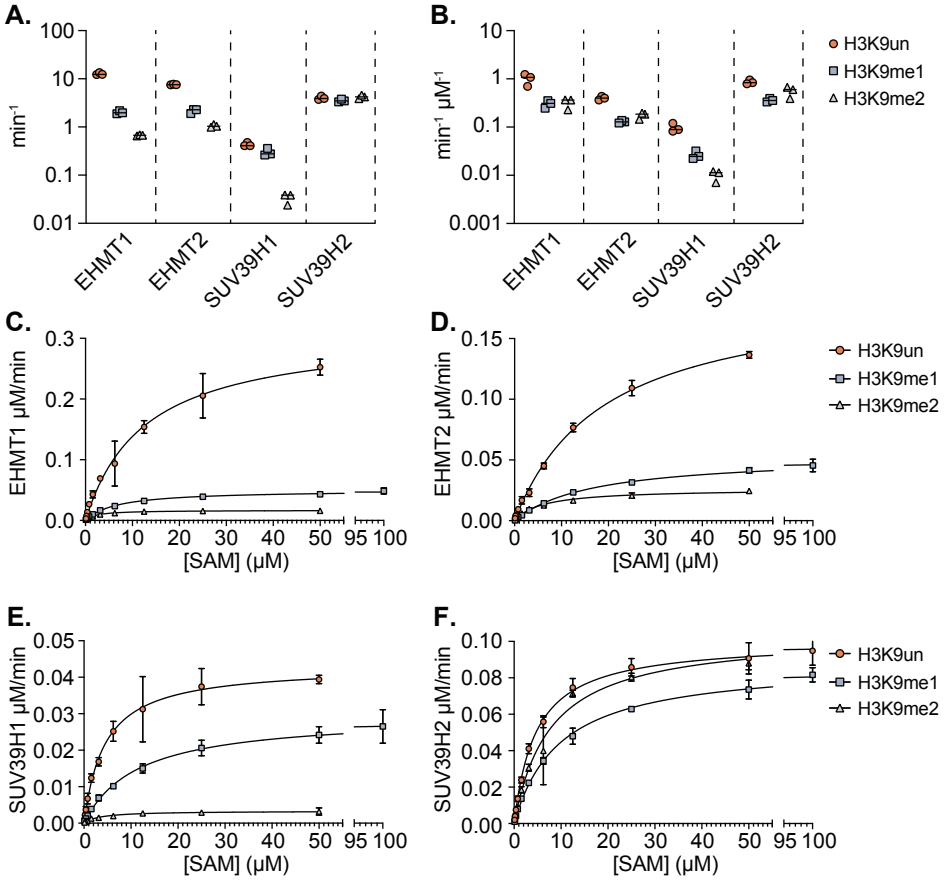

Figure 1: Kinetic analysis of H3K9 HMTs under SAM limiting conditions. Summary plots depicting (*A*) k_{cat} and (*B*) k_{cat}/K_M values derived from steady-state kinetic analysis of EHMT1, EHMT2, SUV39H1, and SUV39H2 when provided with fixed H3(1-17) K9 unmodified (H3K9un), mono-methylated (H3K9me1), or di-methylated (H3K9me2) peptide substrate concentrations and varied SAM concentrations. (*C-F*) Individual steady-state kinetic analyses of EHMT1 (25 nM), EHMT2 (25 nM), SUV39H1 (100 nM), and SUV39H2 (25 nM) under fixed H3(1-17)K9 concentrations (50 μM) and varied SAM concentrations (0.1 - 100 μM) which provided the summary values presented in panels (*A*) and (*B*).

Figure 2: Comparison of HMT $K_{M,\ H3K9X}$ values with nuclear H3K9 proteoform availability.

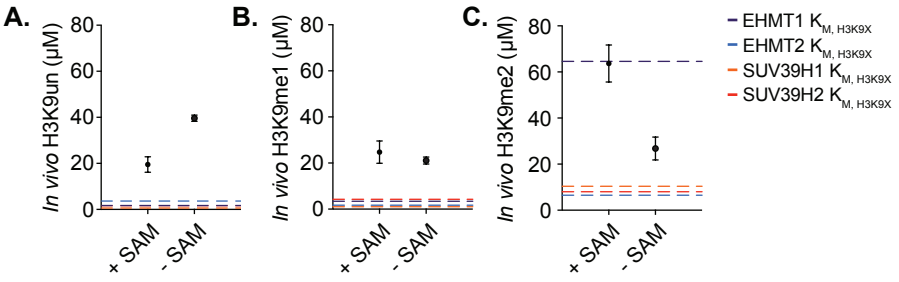

Figure 2: Comparison of HMT $K_{M,\ H3K9X}$ values with nuclear H3K9 proteoform availability. Nuclear (*A*) H3K9 unmodified (H3K9un), (*B*) monomethylated (H3K9me1), and (*C*) dimethylated (H3K9me2) residue concentrations under SAM-replete and -deplete conditions in HCT116 colorectal cancer cells. H3K9 peptide substrate K_M values generated from the kinetic analysis of EHMT1, EHMT2, SUV39H1, and SUV39H2 presented in Figure 3 are superimposed onto each graph to facilitate direct comparison of *in vivo* H3K9 proteoform availability with empirically determined *in vitro* H3K9 peptide proteoform K_M values

Figure 3: Kinetic analysis of H3K9 HMTs under H3 substrate limiting conditions.

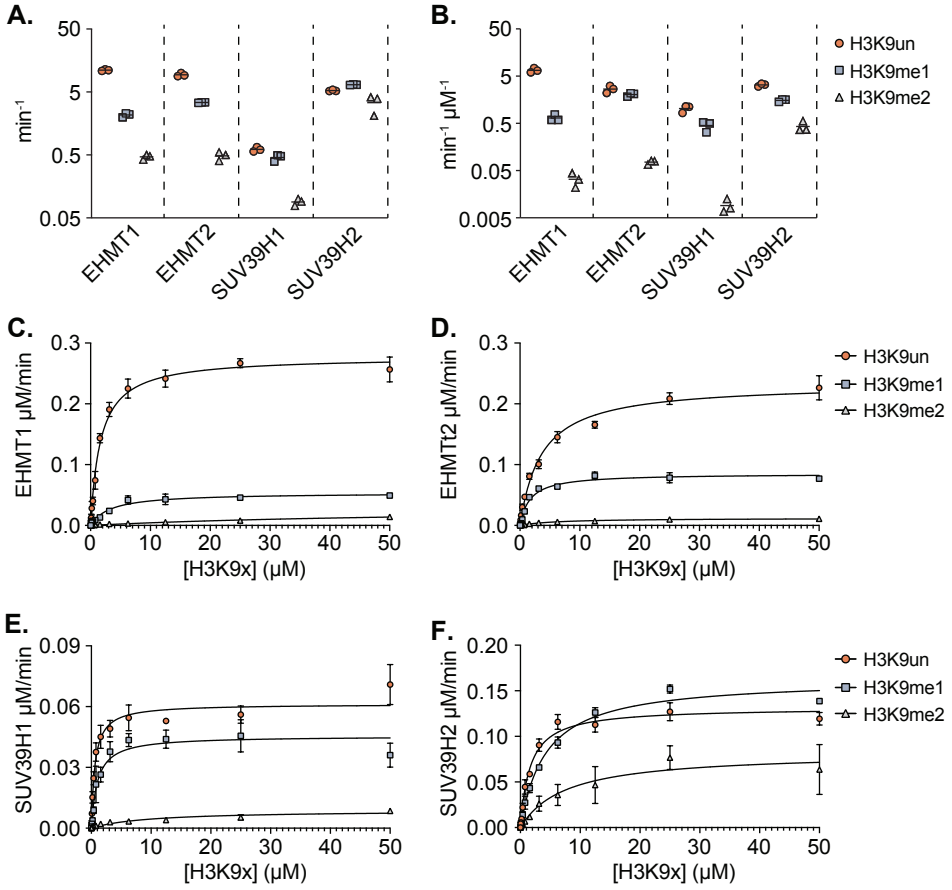

Figure 3: Kinetic analysis of H3K9 HMTs under H3 substrate limiting conditions. Summary plots depicting (*A*) k_{cat} and (*B*) k_{cat}/K_M values derived from steady-state kinetic analysis of EHMT1, EHMT2, SUV39H1, and SUV39H2 when provided with fixed SAM concentrations and varied H3(1-17) K9 unmodified (H3K9un), mono-methylated (H3K9me1), or di-methylated (H3K9me2) peptide substrate concentrations. (*C-F*) Individual steady-state kinetic analyses of EHMT1 (25 nM), EHMT2 (25 nM), SUV39H1 (100 nM), and SUV39H2 (25 nM) under fixed SAM concentrations (50 μM) and varied H3(1-17) K9 peptide concentrations (0.05 - 50 μM) which provided the summary values presented in panels (*A*) and (*B*).

Figure 4: Mathematical modeling of nuclear H3K9 methylation dynamics.

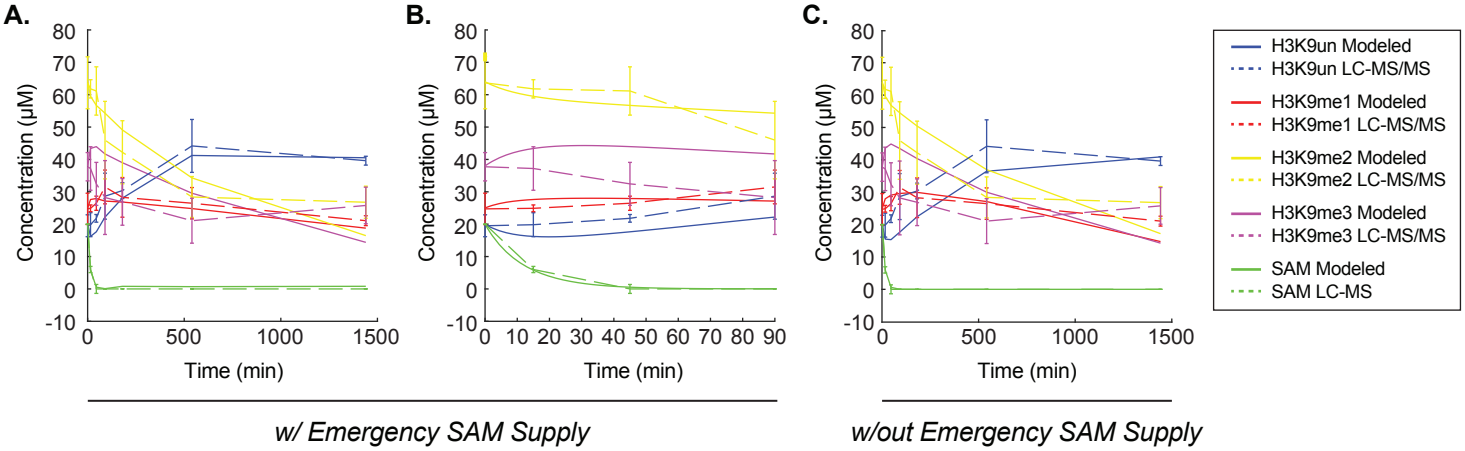

Figure 4: Mathematical modeling of nuclear H3K9 methylation dynamics. (*A*-*C*) Plots depicting changes in H3K9 proteoform and SAM concentrations as measured both empirically via LC-MS-based analyses and by mathematical modeling using the HMT kinetics data generated in this study. A starting SAM concentration of 20 μM was chosen as a representative intracellular value from which relative LC-MS SAM abundance data was converted to μM values. Panels (*A*) and (*B*) display modeled H3K9 proteoform and SAM concentrations under the assumption of an existent emergency SAM supply while the modeled data in panel (*C*) does not include this assumption.